

The Dissociation Rate of Acetylacetonate Ligands Governs the Size of Ferrimagnetic Zinc Ferrite Nanocubes

Aidin Lak,^{*,†} Tamara Kahmann,[‡] Simon Jakob Schaper,[¶] Jaroslava Obel,[§] Frank Ludwig,[‡] Peter Müller-Buschbaum,[¶] and Jan Lipfert^{*,†}

[†]*Department of Physics and Center for NanoScience, LMU Munich, Amalienstr. 54, 80799 Munich, Germany*

[‡]*Institute for Electrical Measurement Science and Fundamental Electrical Engineering, Technische Universität Braunschweig, Hans-Sommer-Str. 66, 38106 Braunschweig, Germany*

[¶]*Lehrstuhl für Funktionelle Materialien, Physik Department, Technische Universität München, James-Frank-Str. 1, 85748 Garching, Germany*

[§]*Department of Chemistry and Pharmacy, Analytical Division, LMU Munich, Butenandtstr. 5-13, 81377 Munich, Germany*

E-mail: lak.aidin@physik.uni-muenchen.de; jan.lipfert@lmu.de

Abstract

Magnetic nanoparticles are critical to a broad range of applications, from medical diagnostics and therapeutics to biotechnological processes and single molecule manipulation. To advance these applications, facile and robust routes to synthesize highly magnetic nanoparticles over a wide size range are needed. Here, we demonstrate that changing the degassing temperature of thermal decomposition of metal acetylacetonate precursors from 90 to 25°C tunes the size of ferrimagnetic $\text{Zn}_x\text{Fe}_{3-x}\text{O}_4$ nanocubes

from 25 to 100 nm, respectively. We show that degassing at 90°C nearly entirely removes acetylacetonate ligands from the reaction, which results in an early formation of monomers and a reaction-controlled growth following LaMer’s model towards small nanocubes. In contrast, degassing at 25°C only partially dissociates acetylacetonate ligands from the metal center and triggers a delayed formation of monomers, which leads to intermediate assembled structures made of tiny irregular crystallites and an eventual formation of large nanocubes via a diffusion-controlled growth mechanism. Using complementary techniques, we determine the substitution fraction x of Zn^{2+} to be in the range of 0.35-0.37. Our method reduces the complexity of the thermal decomposition method by narrowing the synthesis parameter space to a single physical parameter and enables fabrication of highly magnetic and uniform zinc ferrite nanocubes over a broad size range. The resulting particles are promising for a range of applications, from magnetic fluid hyperthermia to actuation of macromolecules.

Introduction

Magnetic nanoparticles show great promise for a range of biomedical applications such as magnetic fluid hyperthermia (MFH), targeted drug delivery, magnetic resonance imaging (MRI), and magnetic particle imaging.¹⁻⁶ The colloidal synthesis of nanoparticles via thermal decomposition of organometallic precursors has significantly advanced nanoparticle-based technologies, as it offers an excellent control over particle size and shape distribution, and crystallinity.⁷⁻¹⁵ Particles with different sizes and magnetic properties are needed depending on the application in mind. Although 25 nm nanoparticles are suitable for magnetic hyperthermia,¹⁶ few hundred nanometers large particles are required for cell separation and magnetic tweezers assays to manipulate cells and macromolecules.¹⁷⁻²⁰

Size controlled synthesis of magnetic nanoparticles up to hundreds of nanometers has been reported previously.^{13,14} Recently, there has been a shift towards synthesizing anisotropically-shaped magnetic particles such as cubic,²¹⁻²⁷ octapod-,^{28,29} and flower-shaped³⁰ particles

instead of spheres. Anisotropic particles have a larger magnetic anisotropy due to an additional contribution from shape anisotropy, a more defined magnetization axis, and a larger surface-to-volume ratio compared to spherical particles with equal volume.³¹ In most studies a combination of chemical synthesis parameters such as the capping ligands and external synthesis parameters like the heating rate was exploited to achieve a wide size range. For instance, in their pioneering work Hyeon and co-workers¹³ have synthesized 160 nm iron oxide nanocubes through thermal decomposition of iron (III) acetylacetonate applying a high heating rate. They have also demonstrated that the particle size reduces to 22 nm if 4-biphenylcarboxylic acid is used in addition to oleic acid. Guardia et al.¹⁴ have shown that the decomposition of the same precursor in the presence of decanoic acid results in large particles only if the heating rate is reduced, in contrast to the results by Hyeon and co-workers. A size increase by applying higher heating rates has recently been shown for other binary oxides.³² In general, the synthesis parameter space of the thermal decomposition method is large and complicated, often resulting in poor reproducibility of the synthesis. In addition, our understanding of the underlying mechanisms through which large nanocubes are formed remains limited.³³

The emergence of iron oxide nanocubes has enabled considerable advancements in e.g. MRI and MFH, yet there is still a high demand for particles with larger magnetization.^{15,16,23,34,35} Approaches to improving the magnetic properties of iron oxide nanoparticles include modifying the reaction's protective gas or the nature of the solvent.³⁶⁻³⁹ However, a more efficient strategy to enhance the saturation magnetization is the replacement of Fe^{3+} with Zn^{2+} in tetrahedral sites of magnetite.⁴⁰⁻⁴³ Although zinc is nonmagnetic, its doping increases the overall magnetization of iron oxide nanoparticles by reducing the antiferromagnetic coupling of Fe^{3+} spins between octahedral and tetrahedral sites through superexchange interactions. Yet, the optimal level of doping x of Zn^{2+} into the tetrahedral sites of $\text{Zn}_x\text{Fe}_{3-x}\text{O}_4$ structure is still controversial.^{41,44,45} In summary, the synthesis of nanocubes with optimized magnetic properties and good size control is very promising to advance nanoparticle-based technolo-

gies, but remains poorly understood.

Here, we demonstrate that the kinetics of colloidal synthesis of $\text{Zn}_x\text{Fe}_{3-x}\text{O}_4$ via thermal decomposition of metal acetylacetonate are governed by dissociation of acetylacetonate ligands and their availability in the reaction. We show that the particle size increases with decreasing degassing temperature due to an increase in the acetylacetonate content of the reaction mixture. The final particles preserve their size uniformity and cubicity regardless of the degassing temperature. We employ complimentary characterization techniques to provide evidence that smaller nanocubes form through a reaction-controlled growth model, whereas large nanocubes grow through assembly of small crystallites into assembled structures and eventual formation of cubic particles, following a diffusion-controlled growth pathway. Our work provides both mechanistic insights and a straight-forward and robust way of synthesizing uniform and highly magnetic zinc ferrite nanocubes suitable for a broad range of biomedical applications.

Results and Discussion

We synthesized zinc ferrite nanoparticles via a colloidal thermal decomposition of iron(III) and zinc(II) acetylacetonate precursors in a mixture of dibenzyl ether as solvent and oleic acid as capping ligands (see the electronic supplementary information (ESI) for details of the synthesis procedure). We systematically varied the degassing temperature of the synthesis reaction as the only variable parameter (Fig. S1a). Characterization of particle size and shape by transmission electron microscopy (TEM) revealed a significant impact of degassing temperature on particle size (Fig. 1a-c). While particles exhibited cubic shapes and overall size uniformity regardless of the degassing temperature, lower degassing temperatures gave rise to significantly larger particles. The size histograms (Fig. 1d) feature a clear major fraction at each temperature as well as a minor fraction. Accordingly, we fit the distributions with a double Gaussian function. The mean particle lateral size L_{ma} of the major particle

fraction increases from 24.1(0.2) to 60.6(1.3) and 96.9(0.5) nm (standard error of the mean) as the degassing temperature reduces from 90 to 60 and 25°C. The minor fractions comprise a 30%, 12%, and 30% of the particles with mean sizes of 31.7(0.9), 47.2(9.5), and 69.3(1.3) nm for small, medium, and large nanocubes, respectively. The standard deviation σ of the Gaussian function fitted to the major size fractions is below 10%, indicating their size monodispersity (Table 1).

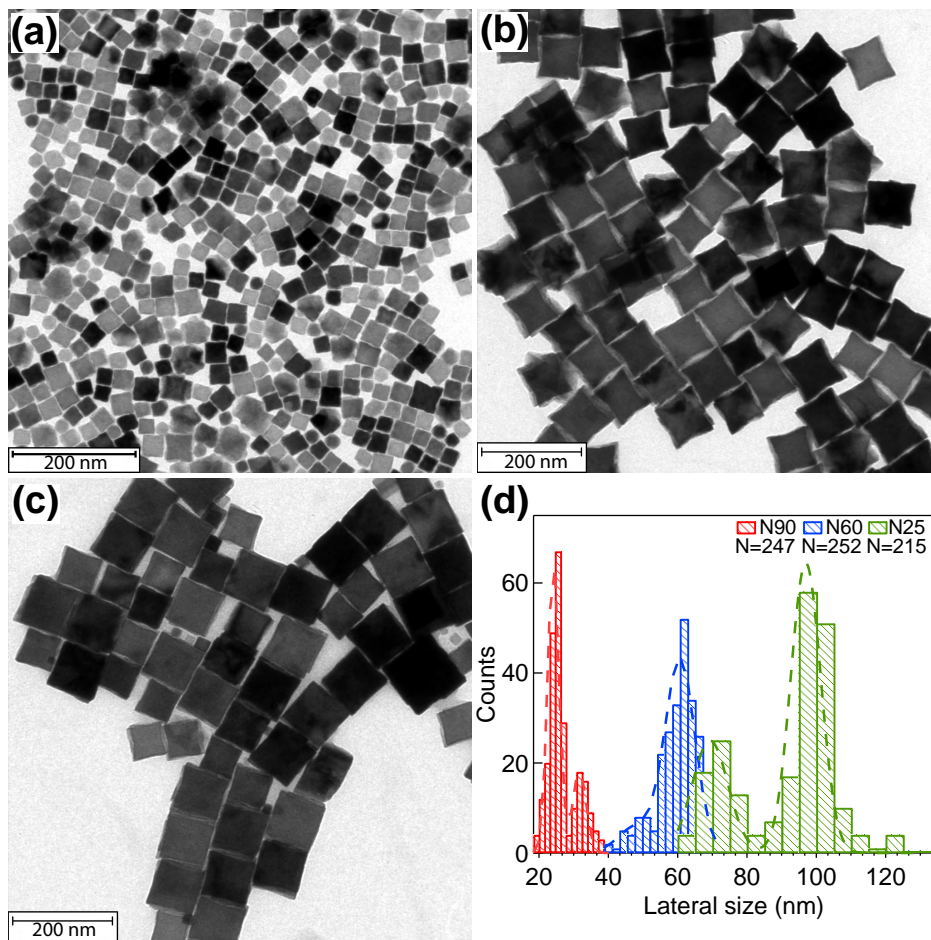


Figure 1: Transmission electron microscopy (TEM) analysis of zinc ferrite nanocubes synthesized after applying three different degassing temperatures. TEM micrographs of zinc ferrite nanocubes synthesized at 290°C after 1 h degassing step at (a) 90°C (N90), (b) 60°C (N60), and (c) 25°C (N25). (d) Histograms of nanoparticle lateral sizes determined from analysis of the TEM images using ImageJ. Dashed lines are double Gaussian fits.

Having observed the very significant impact of the degassing temperature on the particle size, we next probed the chemistry of decomposition reaction to understand the underlying

mechanisms. First, the substances collected in cold trap during the degassing process were analyzed using ^1H NMR spectroscopy.

The analysis of ^1H NMR spectra revealed peaks at 1.89 (G), 5.36 (J), 2.09 (E), and 3.45 (F) ppm that are attributed to enol- and keto-form of acetylacetonate, respectively (Fig. 2). In addition, four minor peaks between 7.46 and 9.94 ppm are observed in the aromatic region of the spectra, which can be assigned to benzaldehyde (BA) (inset of Fig. 2). Therefore, the compounds which were evacuated from the reaction mixture during the degassing process contain metal coordinating acetylacetonate ligands as a major fraction and a trace amount of BA. The total volume extracted from the cold trap V_t increased from 150 to 250 and 450 μL as the degassing temperature increases from 25 to 60 and 90°C. The fraction of acetylacetonate in V_t is given by $\frac{I_{sum}}{1+I_{sum}}$ and was $> 96\%$ for all conditions, with I_{sum} the sum of the integrals of J (1H) and $\frac{1}{2}\times\text{F}$ (2H) peaks at 5.36 and 3.45 ppm. The amounts of extracted acetylacetonate are 89%, 49%, and 29% of the amount initially present (1 mmol Fe(III) acetylacetonate and 1 mmol of Zn(II) acetylacetonate, corresponding to 495 μL total), after degassing at 90, 60, and 25°C, respectively. Therefore, there is a significant difference between the abundance of acetylacetonate in the reaction mixture during the nucleation and growth depending upon the degassing temperature.

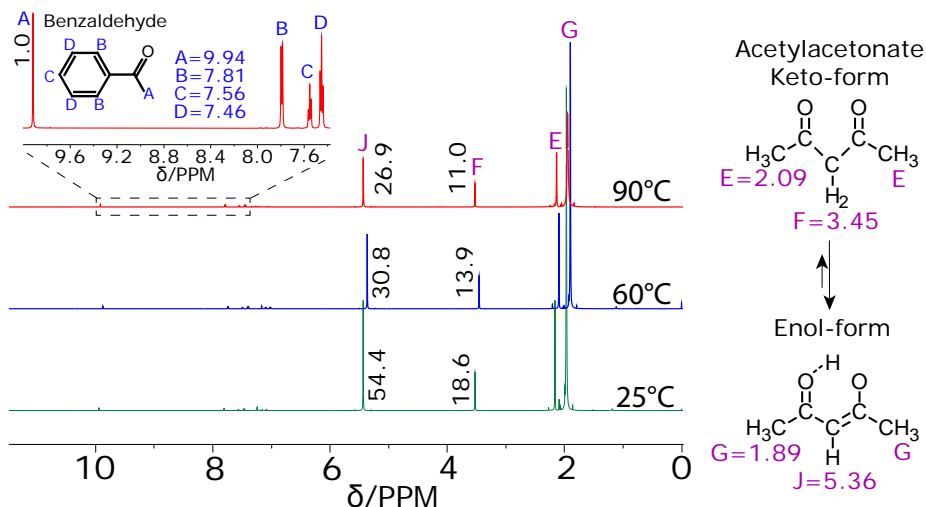


Figure 2: ^1H NMR spectra of substances removed from the reaction mixture during degassing at three different temperatures. ^1H NMR spectra of substances collected in the cold trap after degassing the synthesis mixture for 1 h at different temperatures and a 30 μbar pressure. The inset is a magnification of the aromatic region. All spectra were recorded at 600 MHz on compounds dissolved in CDCl_3 . The integrals are written on the spectra.

To determine the decomposition pathway of the precursor and the role of acetylacetonate ligands on particle formation, we probed the species which are formed at different temperatures and reflux times by attenuated total reflection Fourier-transform infrared (ATR-FTIR) spectroscopy. The FTIR spectra show several absorption bands (Fig. S3 in the ESI), which mostly remain unchanged during the entire reaction and likely stem from DBE and oleic acid. In contrast, several bands in the region from 1500 to 1800 cm^{-1} change drastically during the synthesis reaction (Fig. 3a-c). The bands at 1717 and 1703 cm^{-1} can be assigned to the carbonyl $\text{C}=\text{O}$ stretching vibration. These bands resemble the characteristic double bond of the carbonyl in the acetylacetonate.⁴⁶ We found that the temporal evolution of the carbonyl bands strongly depends on the degassing temperature. In the N90 sample, the acetylacetonate ligands lose their characteristic double band feature already at 260°C (Fig. 3a). At this temperature, an additional broad band at 1693 cm^{-1} appears, which becomes more pronounced up to the reflux temperature and then retreats and disappears as the reflux proceeds. The band at 1693 cm^{-1} plausibly originates from a resonant form of acetylacetonate after disso-

ciation from the metal center. We hypothesize that the dissociation of acetylacetonate and formation of monomers coincide with the time at which the third band emerges.

In the N60 sample (Fig. 3b), the third band at 1693 cm^{-1} appears later in the reaction time, implying a delayed formation of monomers, compared to the N90 condition. Similar to the N90 sample, the band decreases and eventually disappears as the reaction continues. If the degassing temperature is decreased further to 25°C , the bands in the spectral regime around 1700 cm^{-1} exhibit a different temporal evolution compared to the higher degassing temperatures. The double bands of the carbonyl at $1703\text{-}1717\text{ cm}^{-1}$ retain their shape and mostly decrease in intensity during the synthesis reaction. In addition, no band at 1693 cm^{-1} appears during the reaction. Together, the data indicate an even more delayed monomer formation compared to the higher temperatures (Fig. 3c). The evolution of the carbonyl bands for degassing at 25°C looks as if the acetylacetonate ligands remain bound to metal ions throughout the whole reaction, which might suggest that the acetylacetonate binds to metal ions on the particle surface during nucleation and growth of N25 particles.

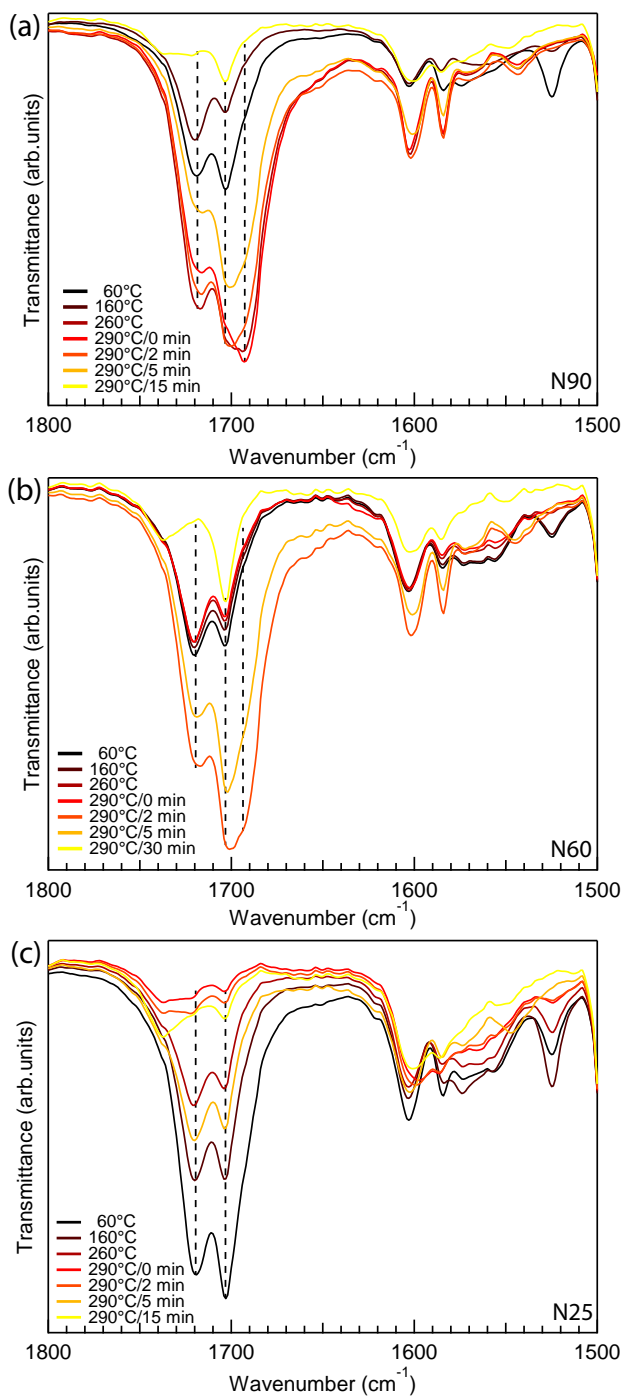


Figure 3: Attenuated total reflection Fourier-transform infrared (ATR-FTIR) spectra of aliquots sampled from the synthesis reaction at different temperatures and reflux times. The temporal evolution of FTIR spectrum recorded on the whole reaction mixture after degassing at (a) 90°C (N90), (b) 60°C (N60), and (c) 25°C (N25). Full spectra are shown in the ESI.

Table 1: Morphological, structural, and magnetic properties of three synthesized samples. Sample name, mean lateral size of the major particle fraction L_{ma} (nm), standard deviation of Gaussian peaks fitted to size histograms σ_{ma} , zinc doping level x from ICP-AES (x_{ICP}) and XRD (x_{XRD}) analyses, particle lattice constant a (Å), Wyckoff atomic position of oxygen $u(O_{32e})$, R_{Bragg} , χ_{global}^2 , reduced remanent magnetization $M_R = M_r/M_s$, and coercive field H_C (mT) derived from TEM, Rietveld analyses, and magnetization measurements.

Name	L_{ma}	σ_{ma}	x_{ICP}^\ddagger	x_{XRD}^\dagger	a^\ddagger	$u(O_{32e})$	R_{Bragg}	χ_{global}^2	M_R	H_C
N90	24.1(0.2)	1.6	0.37	0.25-0.35	8.407	0.2519(4)	3.95	1.36	0.02	4.16(0.13)
N60	60.6(1.3)	4.4	0.37	0.25-0.35	8.400	0.2537(4)	2.06	1.74	0.10	9.13(0.08)
N25	96.9(0.5)	4.3	0.37	0.25-0.35	8.409	0.2530(4)	6.34	2.78	0.22	8.15(0.14)

[†]Amount of iron per unit cell holds 3- x ; [‡]standard errors of a and x_{ICP} are very small and therefore not given; Errors of M_R are less than 1%; numbers given in parentheses are standard error of mean.

To shed light on the effect of dissociation rate of the acetylacetonate on the particle nucleation and growth mechanism, we performed TEM analysis on aliquots taken at different reflux times. For the N90 sample, we observed that a large amount of ≈ 5 nm semi-spherical crystallites are formed after reacting at 290°C for 5 min, suggesting that degassing at 90°C results in an early supersaturation of monomers, leading to a burst nucleation of tiny monodisperse crystallites via LaMer’s nucleation model⁴⁷ (Fig. 4a). By continuing the reaction for 30 min at 290°C, the crystallites grow to cubes with lateral sizes of 24 nm, through a thermodynamically driven shape evolution.⁴⁸ The particle surface area A grows linearly with reflux time t (Fig. 4b), indicating that the growth of the N90 nanocubes is governed by a reaction-controlled growth mechanism.⁴⁹ The burst nucleation mechanism leads to a rapid consumption of monomers, which sets a typical upper particle size limit of ≈ 30 nm.

When the reaction is degassed at 60°C, instead of a burst nucleation, cubic-like assembled structures with mean lateral sizes of ≈ 27 nm seemingly made of irregular crystallites, are formed after refluxing for 5 min (red arrow in Fig. 4c, right side TEM image). These structures grow nearly twice by continuing the reaction for another 10 min, yet having a nonuniform structure (red arrow in Fig. 4c, middle TEM micrograph). As the growth progresses further, the structures transform to well-defined N60 nanocubes. Such a rapid growth rate cannot be described by the reaction-controlled model. Here, the particle volume

V increases linearly with the reflux time t (Fig. 4d), indicating that a diffusion-controlled growth mechanism is dominant.⁴⁹ The diffusion-controlled model is characterized by slow diffusion of monomers towards the particle surface but their quick interaction/accumulation at the surface.

From NMR and FTIR analyses, we found that low temperature degassing results in a higher abundance of the acetylacetonate during the nucleation and growth. Based on the diffusion-controlled model observed for the N60 sample, we hypothesize that the acetylacetonate ligand outcompetes oleic acid in binding to primary crystallites owing to its small size and bidentate binding chemistry. These small ligands on the surface provide the crystallites with an increased surface activity and mobility, and thus trigger their rapid accumulation into assembled structures (Fig. 4c), resulting in the dominance of the diffusion-controlled growth model in the N60 sample. The assembled structures ultimately rearrange themselves into coherent cubes due to high surface activities at 290°C.

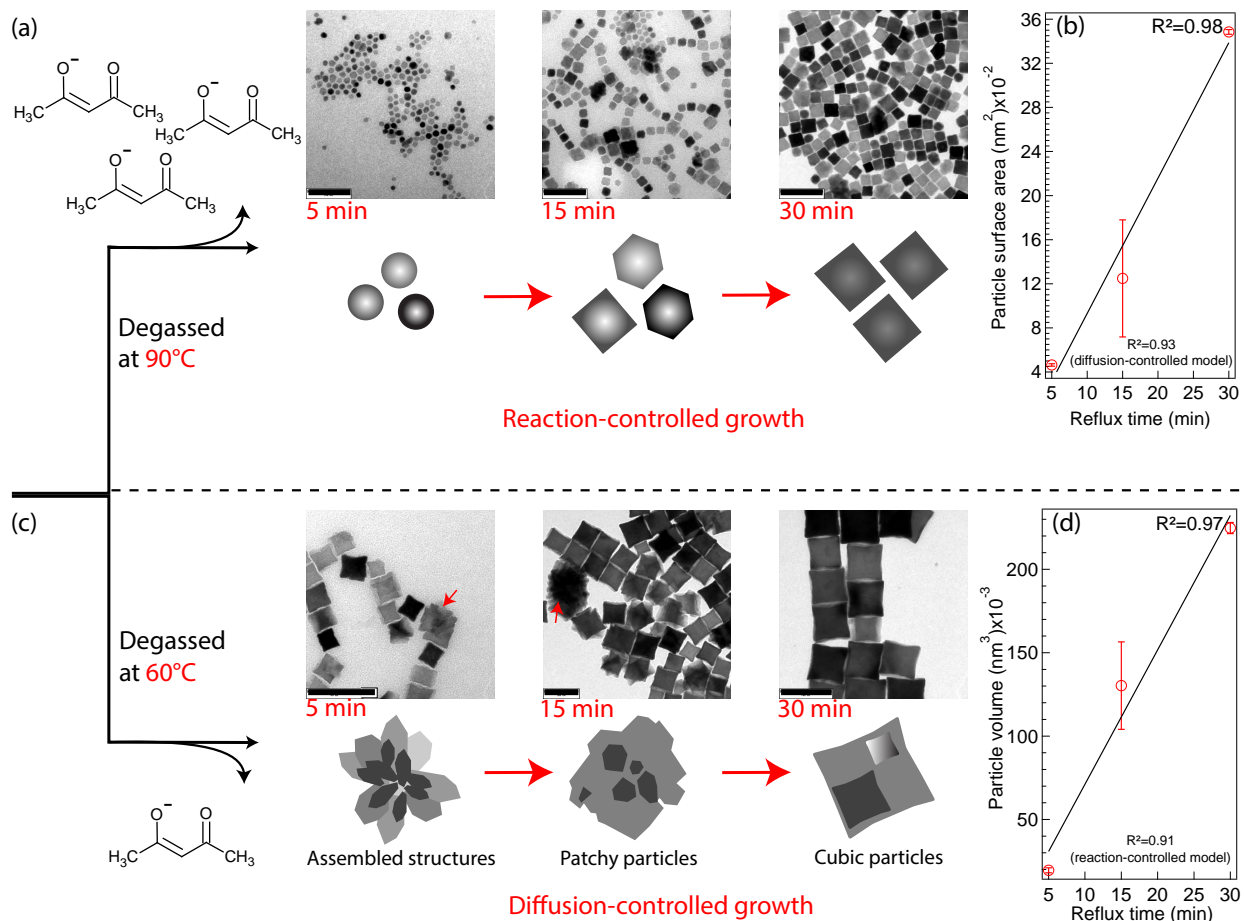


Figure 4: Different particle nucleation and growth models by tuning the degassing temperature, as derived from TEM analyses. (a) Temporal evolution of the particle morphology during refluxing at 290°C for 30 min for the synthesis reaction degassed at 90°C. (b) Particle surface area vs. reflux time at 290°C. (c) Temporal evolution of the particle morphology during refluxing at 290°C for 30 min for the synthesis reaction degassed at 60°C. (d) Particle volume vs. reflux time at 290°C. The TEM scale bars are 100 nm. The particle growth rates are poorly described if the data are fitted to the other respective model, as deduced from lower R^2 .

Since the particle crystal structure and Zn^{2+} distribution in the lattice directly influence the magnetic properties, we next performed powder X-ray diffraction (XRD) analysis. The XRD patterns show sharp and intense reflections, confirming high crystallinity of the synthesized particles (Fig. 5a-c). The reflection positions and relative intensities can be indexed to a single cubic spinel phase for all three samples. The major reflections are labeled in Fig. 5a. No unassigned reflection remains, implying that the insertion of Zn^{2+} into the

lattice did not result in the formation of other crystalline phases. The XRD patterns were analyzed by quantitative Rietveld pattern refinement to obtain the crystal lattice constant a , the site occupancy of Fe^{3+} and Zn^{2+} in tetrahedral sites, and the Wyckoff atomic position of oxygen $u(O_{32e})$ using the Fullprof Suite software.⁵⁰ The patterns were refined assuming an inverse spinel crystal structure with $\text{Fd}\bar{3}m$ space group. The refinement sequence of the fit parameters is described in detail in the ESI.

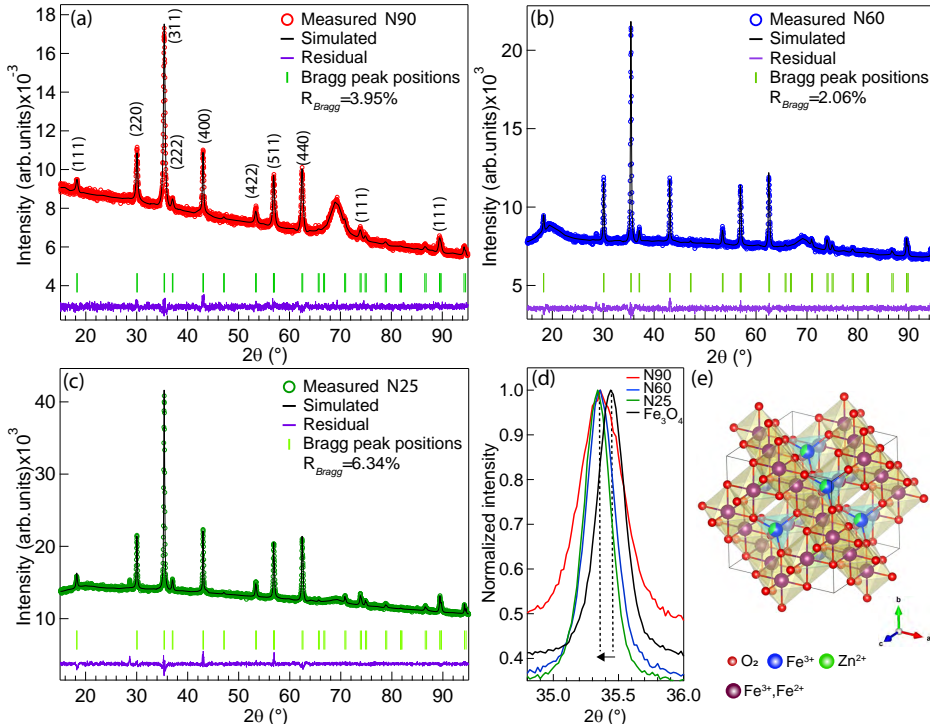


Figure 5: X-ray diffraction patterns and Rietveld pattern refinement analyses. Powder X-ray diffraction patterns of (a) N90, (b) N60, and (c) N25 samples. The simulated patterns based on the Rietveld analysis of XRD patterns, the Bragg peak positions, and the fit residual are co-plotted together with the measured patterns. The broad peak at $2\theta=69^\circ$ is a reflection from the silicon wafer. (d) Comparison between the peak position of the (311) reflection in different samples compared to 200 nm Fe_3O_4 nanocubes synthesized via an otherwise identical synthesis procedure without zinc. (e) Cubic lattice structure of $\text{Zn}_{0.37}\text{Fe}_{2.63}\text{O}_4$ representing Fe^{3+} and Zn^{2+} cations sharing tetrahedral sites and Fe^{3+} and Fe^{2+} occupying octahedral sites.

The best fits to the XRD patterns were obtained by considering larger lattice constants a than magnetite nanocubes i.e. 8.39 \AA^{15} synthesized using an otherwise identical protocol without adding zinc (Table 1). The expansion of a indicates a successful insertion of Zn^{2+}

into the spinel lattice, which is qualitatively manifested in a shift in the XRD peak positions (Fig. 5d). For all three samples, the atom site occupancy of Zn^{2+} and Fe^{3+} in the tetrahedral T_d sites varies between 0.25-0.35 and 0.75-0.65, respectively, as deduced from the Rietveld analyses. The goodness of the Rietveld refinement, determined by R_{Bragg} and χ_{global}^2 , does not change significantly for values within these ranges (Table 1). The uncertainty in the atom site occupancies may originate from similar scattering factor of zinc and iron. However, we note that the goodness-of-fit did worsen by inserting Zn^{2+} in the octahedral sites O_h . The insertion of Zn^{2+} into Fe_3O_4 lattice leads to the substitution of Fe^{3+} in T_d with Zn^{2+} owing to higher affinity of zinc to these crystalline sites. As a result, Fe^{3+} cations migrate to O_h sites. The Wyckoff atomic position of oxygen $u(O_{32e})$ falls within the expected range for a minimally distorted face-centered cubic (fcc) lattice which is 0.255-0.260.⁵¹ The most plausible formula unit of the synthesized nanocubes is therefore $(\text{Zn}^{2+}\text{Fe}^{3+})_x\text{T}_d(\text{Fe}^{3+}\text{Fe}^{2+})_{3-x}\text{T}_d\text{O}_h\text{O}_4$. The zinc concentration estimated from the XRD analysis was on average 20% smaller than ICP-AES elemental analysis, still agreeing within error (Table 1), which plausibly attributes to the fact that in an ICP analysis all existing zinc ions are measured regardless of being embedded in the lattice or being dissolved in the solution upon shelf storage.

To determine how the Zn^{2+} substitution influences the particle magnetization, we recorded field and temperature dependent magnetizations. The saturation magnetization M_s values, here estimated from magnetization M - H curves, are 430, 360, and 620 kA/m for N25, N60, and N100 samples, respectively (Fig. 6a). These values exceed the typical values reported for Fe_3O_4 nanoparticles in literature, varying from 300-450 kA/m,^{15,52} indicating uncompensated Fe^{3+} in O_h sites and effective insertion of Zn^{2+} in T_d sites (Fig. 6c). The N25 nanocubes show an extraordinary high room temperature M_s , which corresponds to 188 emu/ g_{Fe} , provided that $\rho = 5.25$ g/cm³. Taking 124 emu/ g_{Fe} (465 kA/m) as the bulk M_s of magnetite into account, M_s of the N25 nanocubes is ca. 1.5 times higher than that of magnetite. Given the net magnetic moment of a unit cell of a stoichiometric magnetite is 32 μ_B , the net magnetic moment of N25 is 48.5 μ_B per unit cell (Fig. 6c). The estimated

magnetic moment corresponds to a replacement of ≈ 2.8 Fe^{3+} ions in T_d sites with Zn^{2+} , corresponding to a ≈ 0.36 Zn^{2+} occupancy, given that the maximum number of ions per unit cell in T_d sites is 8, in excellent agreement with the values determined from XRD and ICP. The inclusion of Zn^{2+} leads to a smaller improvement in M_s for N90 and N60 samples than N25. Generally, the literature agrees well on maximizing M_s of magnetite by a 0.4-0.5 Zn^{2+} substitution into the lattice. However, most of M_s values reported so far are below what is nominally expected for this amount of substitution^{41-43,45,53} (see the scheme in Fig. 6c). It has recently been shown that a 0.4 Zn^{2+} insertion into 8 nm zinc cobalt ferrite particles causes weakening of the magnetic exchange coupling J between ions in T_d and O_h sites.⁴⁴ A weaker magnetic coupling together with surface and core spin canting,⁵⁴ often present in nanosize magnetic particles, can account for a reduced M_s measured for the N90 and N60 samples.

The coercive fields H_C of N90, N60, and N25 samples are 4.16, 9.13, and 8.15 mT (Fig. 6b), respectively, suggesting a relatively soft magnetic behavior (Table 1). Interestingly, H_C decreases as the size increases from 60 nm to 100 nm, which indicates a transition from single-domain to multi-domain regime within this size range.

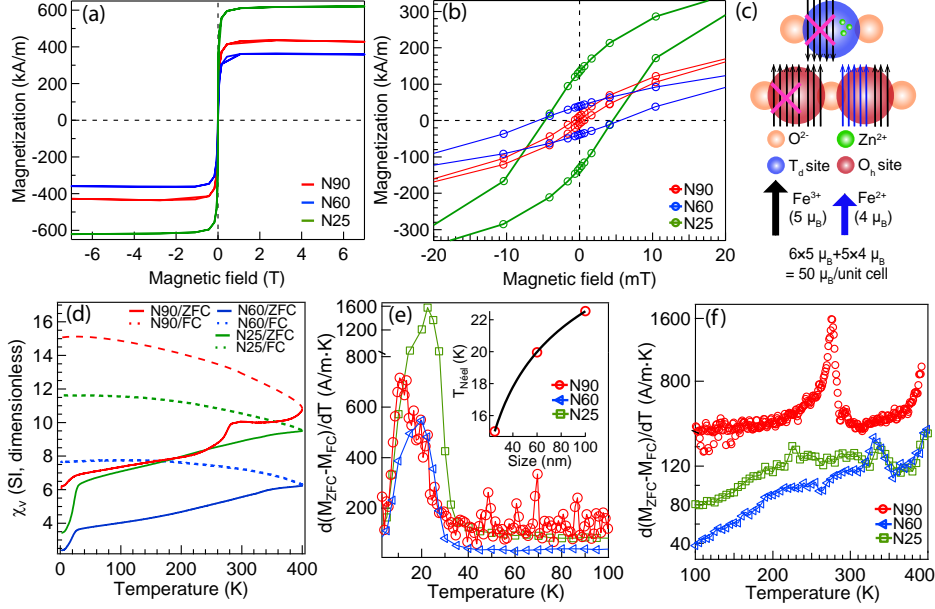


Figure 6: Magnetization as a function of magnetic field and temperature dependent susceptibility measured in a direct current (DC) measurement mode. (a) and (b) Magnetization vs. magnetic field M - H loops of all three samples measured at room temperature. (c) Magnetic spins' configuration of a ferrimagnetic $\text{Zn}_{0.375}\text{Fe}_{2.625}\text{O}_4$ with inverse spinel crystal structure for a unit cell. (d) Volume DC susceptibility measured at 10 mT magnetic fields in zero-field-cooled (ZFC) (solid lines) and field-cooled (FC) (dashed lines) modes vs. temperature. (e) $d(M_{ZFC} - M_{FC})/dT$ vs. T plotted from 2 to 100 K; the inset shows the dependence of the Néel transition temperature on the particle size. The solid line is a guide to the eye. (f) $d(M_{ZFC} - M_{FC})/dT$ vs. T plotted from 100 to 400 K; the solid line is a Gaussian fit.

All three samples reveal a abrupt rise in DC volume susceptibility χ_v measured in zero-field-cooled (ZFC) mode with increasing temperature in the regime below 25 K (Fig. 6d). At temperatures above 25 K, the ZFC curves rise gradually up to 400 K and except N90 nanocubes no other sample reaches a maximum in the temperature regime probed. It is well known that the Verwey transition in magnetite $\text{Fe}_{3-\delta}\text{O}_4$ vanishes even by a minimal iron deficiency $\delta=0.06$ or by doping zinc into the lattice.^{16,45} The absence of a well-defined transition, particle-particle interactions,⁵⁵ and particle size and magnetic energy barrier KV_m distributions can account for a gradual rise of χ_v curves to high temperatures.⁵⁶ Plotting $d(M_{ZFC} - M_{FC})/dT$ vs. temperature T , all three samples show a sharp transition peak between 15 and 24 K (Fig. 6e), shifting to higher temperatures with the particle size. The

transition could originate from both antiferromagnetic Néel transition T_N and geometrical-frustration due to finite size effects,⁵⁷ yet its exact origin is controversial. Similar to our observation, a size dependent Néel transition was reported in MnFe_2O_4 and NiO nanocrystals,^{58,59} and was related to finite size effects. The T_N vs. D data (inset of Fig. 6e), however, cannot be fitted to the Binder finite-scaling⁶⁰ with parameters in a physically plausible range. The poor fit of the Binder model might partially stem from a difference between $T_N(\textit{bulk})$ of our particle composition compared to ZnFe_2O_4 i.e. 10 K.⁵⁷ Unfortunately, the information on the bulk-like behavior of our particle composition is nonexistent, making further discussion on the size dependent behavior speculative. The higher T_N of the N25 particles can also be partially attributed to high degree of Zn^{2+} inversion in the lattice.⁵⁸

A more relevant magnetic transition in magnetic nanoparticles for biological applications is the superparamagnetic (SPM) blocking temperature, above which the particles possess no spontaneous magnetization. Like for the low temperature transition, the SPM blocking temperature T_B of nanoparticles coincides well with the inflection point of the ZFC curve.^{22,56} To evaluate this transition, we plotted the differential curves between 100 and 400 K in a separate panel (Fig. 6f). The N90 sample shows a narrow SPM transition peak with a mean T_B located at 275 K, indicating their superparamagnetic behavior at room temperature. The other two samples show no sign of the SPM transition up to 400 K, which is expected for such particle size.

We found from ^1H NMR spectra recorded on the reaction mixtures at the end of synthesis that a significant amount of benzaldehyde (BA) is formed during the reaction, in particular after degassing at 90°C, likely due to oxidation of DBE by exposed metal centers (Fig. S4, further discussions are given in the ESI). Interestingly, adding 200 μL of reagent grade BA to the N25 sample synthesis reaction after degassing increases the final particle size for about 15 nm (Fig. S5, ESI). These observations suggest that while in our synthesis reactions the acetylacetonate content is the decisive parameter in defining the final particle size, changes in the equilibrium of coordinating ligands can further increase the particle size.

In summary, we have demonstrated very significant influence of the reaction degassing temperature on the kinetics of nucleation and growth of zinc ferrite nanocubes synthesized via thermal decomposition of metal acetylacetonates. We have shown that the particle size can be tuned from 25 to 100 nm simply by reducing the pretreating degassing temperature. We have demonstrated that when the reaction is degassed at 90°C, a major fraction of the acetylacetonate ligands dissociates from metal ions and leaves the reaction vessel, leading to an early nucleation of crystallites, which then follow a reaction-controlled growth pathway. Instead, by degassing at 25°C, the acetylacetonate ligands remain largely associated to metal ions up to high temperatures, resulting in a late decomposition of the precursor. The consequent delayed nucleation and high content of acetylacetonate ligands trigger the formation of assembled structures made of small crystallites, which eventually rapidly grow to large nanocubes following a diffusion-controlled growth mechanism. Our synthetic protocol narrows the complex parameter space of thermal decomposition to a single physical parameter. From technological point of view, our procedure simplifies size controlled synthesis of highly magnetic nanoparticles over a wide size range, which covers a broad range of current biomedical applications, from magnetic fluid hyperthermia and magnetic particle imaging, to cell separation, and manipulation of macromolecules. We envisage that the approach here developed can potentially be extended to other magnetic materials such as iron oxide, manganese doped zinc ferrite, and cobalt ferrite nanoparticles.

Methods

Materials

Iron(III) acetylacetonate (99.8%, metal trace), dibenzyl ether (DBE, 98%), oleic acid (OA, 90%), DMSO-d₆ (99.5 atom % D), CDCl₃ (99.8% atom % D), and solvents with the highest purity grade were purchased from Sigma-Aldrich. Oleic acid (99%) was purchased from TCI, America. Zinc(II) acetylacetonate (95%) was purchased from Merck. The chem-

icals were utilized without further purification.

Synthesis of Nanocubes

In a typical synthesis and to obtain 60 nm zinc ferrite nanocubes, a mixture of 1 mmol (0.353 g) iron(III) acetylacetonate, 1 mmol (0.263 g) zinc(II) acetylacetonate, 10 mL DBE, and 4 mmol (1.26 mL) oleic acid were added into a 50 mL three-necked glass flask, equipped with a thermometer and connected to a Schlenk line through a condenser. The mixture was degassed at 60-70°C and 30 μ bar reducing pressure for 1 h using schlenk techniques. Afterwards, the flask was filled with N₂ and the mixture was heated up to 130°C at a heating ramp rate of 4°C/min and kept for 5 min to thoroughly homogenize the mixture. Subsequently, the mixture was heated up to 290°C at a heating ramp rate of 20°C/min and aged at this temperature for 30 min. After cooling the flask to 80°C, the black viscous product was diluted and dispersed by adding 20 mL of chloroform. The formed particles were precipitated by adding 50 mL of acetone and centrifuging at 7000 rpm for 10 min. After each centrifugation step, the collected particles were dispersed in 20 mL of chloroform through a vigorous 10 min sonication. The washing procedure was repeated five more times to remove organic species and obtain clean particles. Finally, the particles were dispersed in 20 mL of chloroform and stored at room temperature (RT) for further use and characterization. To reduce the particle aggregation and preserve the colloidal stability of the particles during the storage period, 500 μ L of oleic acid was added to suspension. The synthesis experiments for ¹H NMR and FTIR analyses were carried out using oleic acid with a 99% purity.

To obtain 25 and 100 nm nanocubes, the degassing temperature was set to 90 and 25°C, respectively, and other synthesis parameters were kept exactly the same.

Transmission electron microscopy (TEM)

TEM micrographs were acquired on a JEOL JEM-1011 microscope operated at 80 kV. The sample was prepared by dropping a diluted particle suspension in chloroform on a 300 mesh Formvar-carbon coated copper grid and letting it to dry thoroughly. The particle size histogram was analyzed using ImageJ software by taking more than 200 particles into the

analysis.

Magnetization measurements

Field dependent static magnetic measurements were carried out using a Magnetic Property Measurement System (MPMS3, Quantum Design) on embedded nanoparticles. The samples were prepared by mixing 20 μL of a nanocube chloroform solution at an iron concentration of 1-2 g/L with ca. 5 mg of cotton wool in designated capsules and letting it dry thoroughly. The zero-field-cooled (ZFC) and field-cooled (FC) temperature dependent magnetization measurements were performed on the identical samples in magnetic cooling fields of 10 mT. The magnetization data were corrected with respect to the diamagnetic and paramagnetic contributions of cotton wool and capsule. The magnetization curves were normalized to the total mass of zinc ferrite nanoparticles that was estimated from the elemental analysis of zinc and iron.

Elemental analysis

The elemental analysis was performed using an Inductively Coupled Plasma-Atomic Emission Spectroscopy (ICP-AES) instrument (Varian, Vista RL). Typically, 25 μL of a nanocube suspension in chloroform was digested in 1 mL of Aqua Regia (3 parts HCl: 1 part HNO_3) in a 10 mL volumetric flask. The sample was left overnight to fully digest the particles. Afterwards, the flask was filled up to the graduation mark with Milli-Q water and filtered through 0.2 μm filter membrane prior to the measurement.

Powder X-ray diffraction (XRD)

The XRD samples were prepared by drop casting concentrated particle suspensions on a zero diffraction silicon wafer ($\langle 100 \rangle$, 10-20 ohmcm). The measurements were conducted on a D8 Advance Bruker diffractometer, equipped with 9 kW Cu $K\alpha$ rotating anode operating at 40 mA and 40 kV. The patterns were recorded in a parallel beam geometry over an angular range of $2\theta=15^\circ-95^\circ$ in a step size of 0.02° .

Attenuated total reflection Fourier-transform infrared spectroscopy (ATR-FTIR)

The chemical bonds of species formed during the colloidal heat-up synthesis were probed

using ATR-FTIR technique using a Perkin Elmer (Spectrum BX) instrument. The measurements were performed on the whole reaction mixture as sampled out of the reaction without further purification. In a typical measurement, a 10 μL sample drop was placed on the diamond sample holder of the instrument and the spectrum was recorded from 650 to 4400 cm^{-1} .

^1H NMR spectroscopy

The chemical structures of the substances collected in the cold trap after degassing and the reaction mixtures at the end of synthesis were analyzed using ^1H NMR spectroscopy (Varian). The samples were prepared by mixing typically 200 μL of sample with deuterated solvents. The spectra were recorded in CDCl_3 or DMSO-d_6 at 600 MHz.

Supporting Information Available

Rietveld XRD pattern refinement scheme, further discussion on ^1H NMR results, Table S1, Fig. S1, Fig. S2, Fig. S3, Fig. S4, and Fig. S5.

Author Information

Corresponding Authors

*E-mail: lak.aidin@physik.uni-muenchen.de

*E-mail: jan.lipfert@lmu.de

Notes

The authors declare no competing financial interest.

Acknowledgement

We thank Javad Shamsi for fruitful discussions on the reaction chemistry, Jochen Feldmann and Lakshminarayana Polavarapu for access to the synthesis facilities, Petra Keilholz for

help with ^1H NMR measurements, and Tim Liedl and Sussane Kempter for access to the transmission electron microscopy facility. We acknowledge funding from the Alexander von Humboldt Foundation for a postdoctoral research grant to A.L. and from the DFG via the Nanoinitiative Munich (NIM), SFB 863, project A11, Braunschweig International School of Metrology B-IGSM, the DFG Research Training Group 1952 Metrology for Complex Nanosystems.

References

- (1) Pankhurst, Q. A.; Connolly, J.; Jones, S. K.; Dobson, J. Magnetic Nanoparticles: Synthesis, Protection, Functionalization, and Application. *J. Phys. D Appl. Phys.* **2003**, *36*, R167–R181.
- (2) Jeong, U.; Teng, X.; Wang, Y.; Yang, H.; Xia, Y. Superparamagnetic Colloids: Controlled Synthesis and Niche Applications. *Adv. Mater.* **2007**, *19*, 33–60.
- (3) Na, H. B.; Song, I. C.; Hyeon, T. Inorganic Nanoparticles for MRI Contrast Agents. *Adv. Mater.* **2009**, *21*, 2133–2148.
- (4) Krishnan, K. M. Biomedical Nanomagnetism: A Spin Through Possibilities in Imaging, Diagnostics, and Therapy. *IEEE Trans. Magn.* **2010**, *46*, 2523–2558.
- (5) Ho, D. O. N.; Sun, X.; Sun, S. *Acc. Chem. Res.* **2011**, *44*, 875–882.
- (6) Gleich, B.; Weizenecker, J. Tomographic Imaging Using the Nonlinear Response of Magnetic Particles. *Nature* **2005**, *435*, 1214–1217.
- (7) Hyeon, T. Chemical Synthesis of Magnetic Nanoparticles. *Chem. Commun.* **2003**, *8*, 927–934.
- (8) Sun, S.; Zeng, H. Size-controlled Synthesis of Magnetite Nanoparticles. *J. Am. Chem. Soc.* **2002**, *124*, 8204–8205.

- (9) Park, J.; An, K.; Hwang, Y.; Park, J. G.; Hon, H. J.; Kim, J. Y.; Park, J. H.; Hwang, N. M.; Hyeon, T. Ultra-large-scale Syntheses of Monodisperse Nanocrystals. *Nat. Mater.* **2004**, *3*, 891–895.
- (10) Hyeon, T.; Lee, S. S.; park, J.; Chung, Y.; Na, H. B. Synthesis of Highly Crystalline and Monodisperse Maghemite Nanocrystallites without a Size-Selection Process. *J. Am. Chem. Soc.* **2001**, *123*, 12798–12801.
- (11) Redl, F. X.; Black, C. T.; Papaefthymiou, G. C.; Sandstrom, R. L.; Yin, M.; Zeng, H.; Murray, C. B.; O'Brien, S. P. Magnetic, Electronic, and Structural Characterization of Nonstoichiometric Iron Oxides at the Nanoscale. *J. Am. Chem. Soc.* **2004**, *126*, 14583–14599.
- (12) Kovalenko, M. V.; Bodnarchuk, M. I.; Lechner, R. T.; Hesser, G.; Schäffler, F.; ; Heiss, W. Fatty Acid Salts as Stabilizers in Size- and Shape-Controlled Nanocrystal Synthesis: The Case of Inverse Spinel Iron Oxide. *J. Am. Chem. Soc.* **2007**, *129*, 6352–6353.
- (13) Kim, D.; Lee, N.; Park, M.; Kim, B. H.; An, K.; Hyeon, T. Synthesis of Uniform Ferrimagnetic Magnetite Nanocubes. *J. Am. Chem. Soc.* **2009**, *131*, 454–455.
- (14) Guardia, P.; Pérez-Juste, J.; Labarta, A.; Batlle, X.; Liz-Marzán, L. M. Heating Rate Influence on the Synthesis of Iron Oxide Nanoparticles: the Case of Decanoic Acid. *Chem. Commun.* **2010**, *46*, 6108–6110.
- (15) Guardia, P.; Di Corato, R.; Lartigue, L.; Wilhelm, C.; Espinosa, A.; Garcia-Hernandez, M.; Gazeau, F.; Manna, L.; Pellegrino, T. Water-soluble Iron Oxide Nanocubes with High Values of Specific Absorption Rate for Cancer Cell Hyperthermia Treatment. *ACS Nano* **2012**, *6*, 3080–3091.
- (16) Lak, A. et al. Fe²⁺ Deficiencies, FeO Subdomains, and Structural Defects Favor Mag-

- netic Hyperthermia Performance of Iron Oxide Nanocubes into Intracellular Environment. *Nano Lett.* **2018**, *18*, 6856–6866.
- (17) Lipfert, J.; Kerssemakers, J. W. J.; Jager, T. Magnetic Torque Tweezers : Measuring Torsional Stiffness in DNA and RecA-DNA Filaments. *Nat. Methods* **2010**, *7*, 2875–2885.
- (18) Lipfert, J.; Van Oene, M. M.; Lee, M.; Pedaci, F.; Dekker, N. H. Torque Spectroscopy for the Study of Rotary Motion in Biological Systems. *Chem. Rev.* **2015**, *115*, 1449–1474.
- (19) Moerland, C. P.; van IJzendoorn, L. J.; Prins, M. W. J. Rotating Magnetic Particles for Lab-on-Chip Applications – a Comprehensive Review. *Lab Chip* **2019**, *19*, 919–933.
- (20) Kim, J.-w.; Jeong, H.-k.; Southard, K. M.; Jun, Y.-w.; Cheon, J. Magnetic Nanotweezers for Interrogating Biological Processes in Space and Time. *Acc. Chem. Res.* **2018**,
- (21) Shavel, A.; Rodríguez-González, B.; Spasova, M.; Farle, M.; Liz-Marzán, L. M. Synthesis and Characterization of Iron/Iron Oxide Core/Shell Nanocubes. *Adv. Funct. Mater.* **2007**, *17*, 3870–3876.
- (22) Pichon, B. P.; Gerber, O.; Lefevre, C.; Florea, I.; Fleutot, S.; Baaziz, W.; Pauly, M.; Ohlmann, M.; Ulhaq, C.; Ersen, O.; Pierron-Bohnes, V.; Panissod, P.; Drillon, M.; Begin-Colin, S. Microstructural and Magnetic Investigations of Wüstite-Spinel Core-Shell Cubic-Shaped Nanoparticles. *Chem. Mater.* **2011**, *23*, 2886–2900.
- (23) Lee, N.; Choi, Y.; Lee, Y.; Park, M.; Moon, W. K.; Choi, S. H.; Hyeon, T. Water-Dispersible Ferrimagnetic Iron Oxide Nanocubes with Extremely High r_2 Relaxivity for Highly Sensitive in Vivo MRI of Tumors. *Nano Lett.* **2012**, *12*, 3127–3131.
- (24) Wetterskog, E.; Tai, C.-W.; Grins, J.; Bergström, L.; Salazar-Alvarez, G. Anomalous Magnetic Properties of Nanoparticles Arising from Defect Structures: Topotaxial Ox-

- idation of $\text{Fe}_{1-x}\text{O}|\text{Fe}_{3-\delta}\text{O}_4$ Core|Shell Nanocubes to Single-Phase Particles. *ACS Nano* **2013**, *7*, 7132–7144.
- (25) Walter, A.; Billotey, C.; Garofalo, A.; Ulhaq-Bouillet, C.; Lefèvre, C.; Taleb, J.; Laurent, S.; Elst, L. V.; Muller, R. N.; Lartigue, L.; Gazeau, F.; Felder-Flesch, D.; Begin-Colin, S. Mastering the Shape and Composition of Dendronized Iron Oxide Nanoparticles To Tailor Magnetic Resonance Imaging and Hyperthermia. *Chem. Mater.* **2014**, *26*, 5252–5264.
- (26) Feld, A.; Weimer, A.; Kornowski, A.; Winckelmans, N.; Merkl, J.-P.; Kloust, H.; Zierold, R.; Schmidtke, C.; Schotten, T.; Riedner, M.; Bals, S.; Weller, H. Chemistry of Shape-Controlled Iron Oxide Nanocrystal Formation. *ACS Nano* **2019**, *13*, 152–162.
- (27) Cotin, G.; Kiefer, C.; Perton, F.; Ihiawakrim, D.; Blanco-Andujar, C.; Moldovan, S.; Lefevre, C.; Ersen, O.; Pichon, B.; Mertz, D.; Bégin-Colin, S. Unravelling the Thermal Decomposition Parameters for The Synthesis of Anisotropic Iron Oxide Nanoparticles. **2018**, *8*, 881.
- (28) Bronstein, L. M.; Atkinson, J. E.; Malyutin, A. G.; Kidwai, F.; Stein, B. D.; Morgan, D. G.; Perry, J. M.; Karty, J. a. Nanoparticles by Decomposition of Long Chain Iron Carboxylates: From Spheres to Stars and Cubes. *Langmuir* **2011**, *27*, 3044–3050.
- (29) Zhao, Z.; Zhou, Z.; Bao, J.; Wang, Z.; Hu, J.; Chi, X.; Ni, K.; Wang, R.; Chen, X.; Chen, Z.; Gao, J. Octapod Iron Oxide Nanoparticles as High-performance T_2 Contrast Agents for Magnetic Resonance Imaging. *Nat. Commun.* **2013**, *4*, 1–7.
- (30) Gavilán, H. et al. Colloidal Flower-Shaped Iron Oxide Nanoparticles: Synthesis Strategies and Coatings. *Part. Part. Syst. Char.* **2017**, *34*, 1700094.
- (31) Salazar-Alvarez, G.; Qin, J.; Šepelák, V.; Bergmann, I.; Vasilakaki, M.; Trohidou, K. N.; Ardisson, J. D.; Macedo, W. A. A.; Mikhaylova, M.; Muhammed, M.; Baró, M. D.;

- Nogués, J. Cubic versus Spherical Magnetic Nanoparticles: The Role of Surface Anisotropy. *J. Am. Chem. Soc.* **2008**, *130*, 13234–13239.
- (32) Muro-Cruces, J.; Roca, A. G.; López-Ortega, A.; Fantechi, E.; del Pozo-Bueno, D.; Estradé, S.; Peiró, F.; Sepúlveda, B.; Pineider, F.; Sangregorio, C.; Nogues, J. Precise Size Control of the Growth of Fe₃O₄ Nanocubes over a Wide Size Range Using a Rationally Designed One-Pot Synthesis. *ACS Nano* **0**, *0*, null.
- (33) Kwon, S. G.; Piao, Y.; Park, J.; Angappane, S.; Jo, Y.; Hwang, N.-m.; Park, J.-g.; Hyeon, T. Kinetics of Monodisperse Iron Oxide Nanocrystal Formation by “ Heating-Up ” Process. *J. Am. Chem. Soc.* **2007**,
- (34) Lee, N.; Kim, H.; Choi, S. H.; Park, M.; Kim, D.; Kim, H.-C.; Choi, Y.; Lin, S.; Kim, B. H.; Jung, H. S.; Kim, H.; Park, K. S.; Moon, W. K.; Hyeon, T. Magnetosome-Like Ferrimagnetic Iron Oxide Nanocubes for Highly Sensitive MRI of Single Cells and Transplanted Pancreatic Islets. *Proc. Natl. Acad. Sci. U. S. A.* **2011**, *108*, 2662–2667.
- (35) Nemati, Z.; Alonso, J.; Rodrigo, I.; Das, R.; Garaio, E.; García, J. n.; Orue, I.; Phan, M.-H.; Srikanth, H. Improving the Heating Efficiency of Iron Oxide Nanoparticles by Tuning Their Shape and Size. *J. Phys. Chem. C.* **2018**, *122*, 2367–2381.
- (36) Hufschmid, R.; Arami, H.; Ferguson, R. M.; Gonzales, M.; Teeman, E.; N.Brush, L.; Browning, N. D.; Krishnan, K. M. Synthesis of Phase-Pure and Monodisperse Iron Oxide Nanoparticles by Thermal Decomposition. *Nanoscale* **2015**, *7*, 11142–11154.
- (37) Kemp, S. J.; Ferguson, R. M.; Khandhar, A. P.; Krishnan, K. M. Monodisperse Magnetite Nanoparticles with Nearly Ideal Saturation Magnetization. *RSC Adv.* **2016**, *6*, 77452–77464.
- (38) Unni, M.; Uhl, A. M.; Savliwala, S.; Savitzky, B. H.; Dhavalikar, R.; Garraud, N.; Arnold, D. P.; Kourkoutis, L. F.; Andrew, J. S.; Rinaldi, C. Thermal Decomposition

- Synthesis of Iron Oxide Nanoparticles with Diminished Magnetic Dead Layer by Controlled Addition of Oxygen. *ACS Nano* **2017**, *11*, 2284–2303.
- (39) Chen, R.; Christiansen, M. G.; Sourakov, A.; Mohr, A.; Matsumoto, Y.; Okada, S.; Jasanoff, A.; Anikeeva, P. High-Performance Ferrite Nanoparticles through Nonaqueous Redox Phase Tuning. *Nano Lett.* **2016**, *16*, 1345–1351.
- (40) Jang, J. T.; Nah, H.; Lee, J. H.; Moon, S. H.; Kim, M. G.; Cheon, J. Critical Enhancements of MRI Contrast and Hyperthermic Effects by Dopant-Controlled Magnetic Nanoparticles. *Angew. Chemie - Int. Ed.* **2009**, *48*, 1234–1238.
- (41) Yang, Y.; Liu, X.; Yang, Y.; Xiao, W.; Li, Z.; Xue, D.; Li, F.; Ding, J. Synthesis of Nonstoichiometric Zinc Ferrite Nanoparticles with Extraordinary Room Temperature Magnetism and their Diverse Applications. *J. Mater. Chem. C* **2013**, *1*, 2875–2885.
- (42) Byrne, J. M.; Coker, V. S.; Cespedes, E.; Wincott, P. L.; Vaughan, D. J.; Pattrick, R. A. D.; van der Laan, G.; Arenholz, E.; Tuna, F.; Bencsik, M.; Lloyd, J. R.; Telling, N. D. Biosynthesis of Zinc Substituted Magnetite Nanoparticles with Enhanced Magnetic Properties. *Advanced Functional Materials* **2014**, *24*, 2518–2529.
- (43) Bauer, L. M.; Situ, S. F.; Griswold, M. A.; Samia, A. C. S. High-Performance Iron Oxide Nanoparticles for Magnetic Particle Imaging-Guided Hyperthermia (hMPI). *Nanoscale* **2016**, *8*, 12162–12169.
- (44) Albino, M.; Fantechi, E.; Innocenti, C.; López-Ortega, A.; Bonanni, V.; Campo, G.; Pineider, F.; Gurioli, M.; Arosio, P.; Orlando, T.; Bertoni, G.; de Julián Fernández, C.; Lascialfari, A.; Sangregorio, C. Role of Zn²⁺ Substitution on the Magnetic, Hyperthermic, and Relaxometric Properties of Cobalt Ferrite Nanoparticles. *J. Phys. Chem. C* **2019**, *123*, 6148–6157.
- (45) Fontaiña-Troitiño, N.; Ramos-Docampo, M. A.; Testa-Anta, M.; Rodríguez-González, B.; Bañobre-López, M.; Bocher, L.; McKenna, K. P.; Salgueiriño, V. An-

- tiphase Boundaries in Truncated Octahedron-Shaped Zn-Doped Magnetite Nanocrystals. *J. Mater. Chem. C* **2018**, *6*, 12800–12807.
- (46) R.M. Silverstein, D. K., F. Webster *Spectrometric Identification of Organic Compounds*, seventh ed.; Wiley: Hoboken, NJ, 1981.
- (47) LaMer, V. K.; Dinegar, R. H. Theory, Production and Mechanism of Formation of Monodispersed Hydrosols. *J. Am. Chem. Soc.* **1950**, *72*, 4847–4854.
- (48) Qiao, L.; Fu, Z.; Li, J.; Ghosen, J.; Zeng, M.; Stebbins, J.; Prasad, P. N.; Swihart, M. T. Standardizing Size- and Shape-Controlled Synthesis of Monodisperse Magnetite Fe₃O₄ Nanocrystals by Identifying and Exploiting Effects of Organic Impurities. *ACS Nano* **2017**, *11*, 6370–6381.
- (49) Sarma, R. V. D. D. In *Nanomaterials Chemistry: Recent Developments and New Directions*; C. N. R. Rao, a. A. K. C., A. Müller, Ed.; Wiley-VCH Verlag GmbH & Co. KGaA: Weinheim, 2007; Chapter 4, pp 139–170.
- (50) Rodriguez-Carvajal, J. *FullProf Suite*; LLB Saclay & LCSIM: Rennes, France, 2003.
- (51) Andersen, H. L.; Saura-Múzquiz, M.; Granados-Miralles, C.; Canévet, E.; Lock, N.; Christensen, M. Crystalline and Magnetic Structure–Property Relationship in Spinel Ferrite Nanoparticles. *Nanoscale* **2018**, *10*, 14902–14914.
- (52) Roca, a. G.; Morales, M. P.; O’Grady, K.; Serna, C. J. Structural and Magnetic Properties of Uniform Magnetite Nanoparticles Prepared by High Temperature Decomposition of Organic Precursors. *Nanotechnology* **2006**, *17*, 2783–2788.
- (53) Park, J.; Porter, M. D.; Granger, M. C. Silica Encapsulation of Ferrimagnetic Zinc Ferrite Nanocubes Enabled by Layer-by-Layer Polyelectrolyte Deposition. *Langmuir* **2015**, *31*, 3537–3545.

- (54) Morales, M. P.; Serna, C. J.; Bødker, F.; Mørup, S. Spin Canting due to Structural Disorder in Maghemite. *J. Phys. Condens. Matter* **1997**, *9*, 5461–5467.
- (55) Lak, A.; Kraken, M.; Ludwig, F.; Kornowski, A.; Eberbeck, D.; Sievers, S.; Litterst, F. J.; Weller, H.; Schilling, M. Size dependent structural and magnetic properties of FeO-Fe₃O₄ nanoparticles. *Nanoscale* **2013**, *5*, 12286–12295.
- (56) Livesey, K. L.; Ruta, S.; Anderson, N. R.; Baldomir, D.; Cahntrell, R. W.; Serantes, D. Beyond the Blocking Model to Fit Nanoparticle ZFC/FC Magnetisation Curves. *Sci. Rep.* **2018**, *8*, 11166.
- (57) Kamazawa, K.; Tsunoda, Y.; Kadowaki, H.; Kohn, K. Magnetic Neutron Scattering Measurements on a Single Crystal of Frustrated ZnFe₂O₄. *Phys. Rev. B - Condens. Matter Mater. Phys.* **2003**, *68*, 3–4.
- (58) Raghavender, A.; Hong, N. H. Dependence of Néel Temperature on the Particle Size of MnFe₂O₄. *J. Magn. Magn.c Mater.* **2011**, *323*, 2145 – 2147.
- (59) Rinaldi-Montes, N.; Gorria, P.; Martínez-Blanco, D.; Fuertes, A. B.; Puente-Orench, I.; Olivi, L.; Blanco, J. A. Size Effects on the Néel Temperature of Antiferromagnetic NiO Nanoparticles. *AIP Adv.* **2016**, *6*, 056104.
- (60) Binder, K. Statistical Mechanics of Finite Three-Dimensional Ising Models. *Physica* **1972**, *62*, 508–526.

TOC Graphic

